remote sensing

MDPI

Article

Rapid Assessment of Landslide Dynamics by UAV-RTK Repeated Surveys Using Ground Targets: The Ca' Lita Landslide (Northern Apennines, Italy)

Giuseppe Ciccarese [1], Melissa Tondo [2,*], Marco Mulas [2], Giovanni Bertolini [3] and Alessandro Corsini [2]

[1] Department of Biological, Geological and Environmental Sciences, University of Bologna, Via Zamboni, 67, 40126 Bologna, Italy; giuseppe.ciccarese2@unibo.it
[2] Department of Chemical and Geological Sciences, University of Modena and Reggio Emilia, Via Giuseppe Campi 103, 41125 Modena, Italy; marco.mulas@unimore.it (M.M.); alessandro.corsini@unimore.it (A.C.)
[3] Reggio Emilia Office, Emilia-Romagna Regional Agency for Territorial Security and Civil Protection, Via Emilia Santo Stefano 25, 42121 Reggio Emilia, Italy; giovanni.bertolini@regione.emilia-romagna.it
* Correspondence: melissa.tondo@unimore.it

Abstract: The combined use of Uncrewed Aerial Vehicles (UAVs) with an integrated Real Time Kinematic (RTK) Global Navigation Satellite System (GNSS) module and an external GNSS base station allows photogrammetric surveys with centimeter accuracy to be obtained without the use of ground control points. This greatly reduces acquisition and processing time, making it possible to perform rapid monitoring of landslides by installing permanent and clearly recognizable optical targets on the ground. In this contribution, we show the results obtained in the Ca' Lita landslide (Northern Apennines, Italy) by performing multi-temporal RTK-aided UAV surveys. The landslide is a large-scale roto-translational rockslide evolving downslope into an earthslide–earthflow. The test area extends 60×10^3 m^2 in the upper track zone, which has recently experienced two major reactivations in May 2022 and March 2023. A catastrophic event took place in May 2023, but it goes beyond the purpose of the present study. A total of eight UAV surveys were carried out from October 2020 to March 2023. A total of eight targets were installed transversally to the movement direction. The results, in the active portion of the landslide, show that between October 2020 and March 2023, the planimetric displacement of targets ranged from 0.09 m (in the lateral zone) to 71.61 m (in the central zone). The vertical displacement values ranged from -2.05 to 5.94 m, respectively. The estimated positioning errors are 0.01 (planimetric) and 0.03 m (vertical). The validation, performed by using data from a permanent GNSS receiver, shows maximum differences of 0.18 m (planimetric) and 0.21 m (vertical). These results, together with the rapidity of image acquisition and data processing, highlight the advantages of using this rapid method to follow the evolution of relatively rapid landslides such as the Ca' Lita landslide.

Keywords: earthslides–earthflows; UAV-RTK; visual tracking; Structure from Motion

Citation: Ciccarese, G.; Tondo, M.; Mulas, M.; Bertolini, G.; Corsini, A. Rapid Assessment of Landslide Dynamics by UAV-RTK Repeated Surveys Using Ground Targets: The Ca' Lita Landslide (Northern Apennines, Italy). *Remote Sens.* **2024**, *16*, 1032. https://doi.org/10.3390/rs16061032

Academic Editor: Michele Saroli

Received: 17 January 2024
Revised: 6 March 2024
Accepted: 12 March 2024
Published: 14 March 2024

1. Introduction

Landslide monitoring requires long-term measurements of vertical and horizontal displacements and pore-water pressure, which are essential for understanding landslide mechanisms and even predicting future movements [1–5]. Ground-based geotechnical and geophysical surveys, which are often conducted to monitor and characterize the evolution of landslides [6–8], provide locally discrete observations and are therefore affected by a limited spatial coverage [9,10].

Since the early 2000s, the development of new techniques led to a revolution in the field of landslide study allowing potentially all researchers to work with Digital Elevation Models (DEMs), remote sensing and numerical modeling [11,12]. Recently, it has become quite usual to implement landslide monitoring systems based on Robotic Total Stations

(RTSs) [13–15] or Global Navigation Satellite Systems (GNSSs) [16] in order to retrieve long-term displacement datasets. Other techniques can be applied for a multi-temporal analysis; that is the case for airborne vehicles equipped with Light Detection and Ranging (LiDAR) sensors [17–20], satellite Synthetic Aperture Radar (SAR) interferometry [21–28] or SAR-based amplitude analysis [29,30] and Terrestrial Laser Scanners (TLSs) [31–33]. Although they have both advantages and disadvantages, these techniques usually can provide near-real-time results and allow large parts of the landslides to be monitored. Recently, the usage of Uncrewed Aerial Vehicles (UAVs) for landslide analysis has become quite common in the natural hazard scientific community [34–36]. The use of UAVs (otherwise known also as Remotely Piloted Aircraft Systems, RPASs) proved efficient even when using off-the-shelf commercial models [37]. The diffusion of Structure from Motion(SfM)-based software tools, has allowed researchers to obtain digital 3D models starting from UAV optical acquisitions [38–41] or even by smartphone cameras [42]. Therefore, this technology started to be adopted in landslide monitoring [43,44]. One of the limitations of UAV surveys equipped with consumer-grade GNSS receivers is the requirement for Ground Control Points (GCPs) to improve the positioning accuracy and precision. This issue was solved by using double-frequency (L1, L2) GNSS receivers on board UAVs. Consequently, at present, it is possible to rapidly acquire data characterized by centimetric accuracy by using a UAV platform without the need for GCPs and therefore without the burden of walking within hazardous areas [45–51]. The goal of this contribution is to present a workflow that allows us to rapidly perform an assessment of landslide dynamics even during acceleration phases. It consists of permanently installing optical targets that can be clearly recognized in repeated successive surveys on the ground to derive displacement time series. We show the results obtained in the Ca' Lita landslide (Northern Apennines, Italy) by performing repeated surveys using a DJI Phantom 4 RTK (drone) and a D-RTK 2 mobile station (double-frequency GNSS receiver) considered as the base station for RTK correction casting. The proposed method proved to be suitable for evidencing the complex and rapid dynamics of the investigated portion of the Ca' Lita landslide that is composed of an earthslide/earthflow with rates of displacements ranging from millimeters per day to meters per day.

2. Case Study

The Ca' Lita landslide is located near the Secchia River, in the Northern Apennines within the Reggio Emilia Province (Emilia-Romagna Region, Northern Italy; Figure 1). According to the classification of Cruden and Varnes [52], it is a complex landslide composed of a roto-translation rockslide in its head zone, mainly constituted of Cretaceous to Eocene flysch rock masses, evolving downslope into a translational earthslide–earthflow made up of chaotic clayey complexes and debris resulting from the degradation of flysch rock masses [53,54]. The landslide develops from north-west to south-east, and its elevation ranges from 650 m to 230 m. It has a total length of nearly 3 km, a maximum width of up to 1.4 km and a maximum depth of the sliding surface of about 42 m, as measured by inclinometers located in the source area [53,55]. On the basis of data retrieved during the last 29 years (1991–2020) by the meteorological station of Baiso, located 4.5 km away from the landslide and approximately at the same elevation, the area of Ca' Lita is characterized by a monthly mean precipitation of around 68.5 mm and a monthly mean temperature of around 12.25 °C [56,57]. Therefore, the area can be classified as a warm temperate climate (Cfa), following Köppen's climatic classification [58].

After several slope instability events occurred during the 1900s, the landslide underwent a period of inactivity until 2004 when a paroxysmal reactivation caused the mobilization of almost 20 million m^3 of mixed clays and boulders, the advancement of the toe of about 400 m at peak velocities of 10 m/day and a significant retrogression of the main crown [53,59,60]. After the 2004 disastrous event, permanent mitigation structures were implemented in the landslide [54,60]. They consisted of draining trenches, draining wells, check dams and pile-funded anchored retaining walls, mostly completed by 2011 [53].

Detailed analyses of groundwater levels and chemistry proved the existence of a strong relationship between deep-groundwater inflow and the evolution of the landslide [60,61].

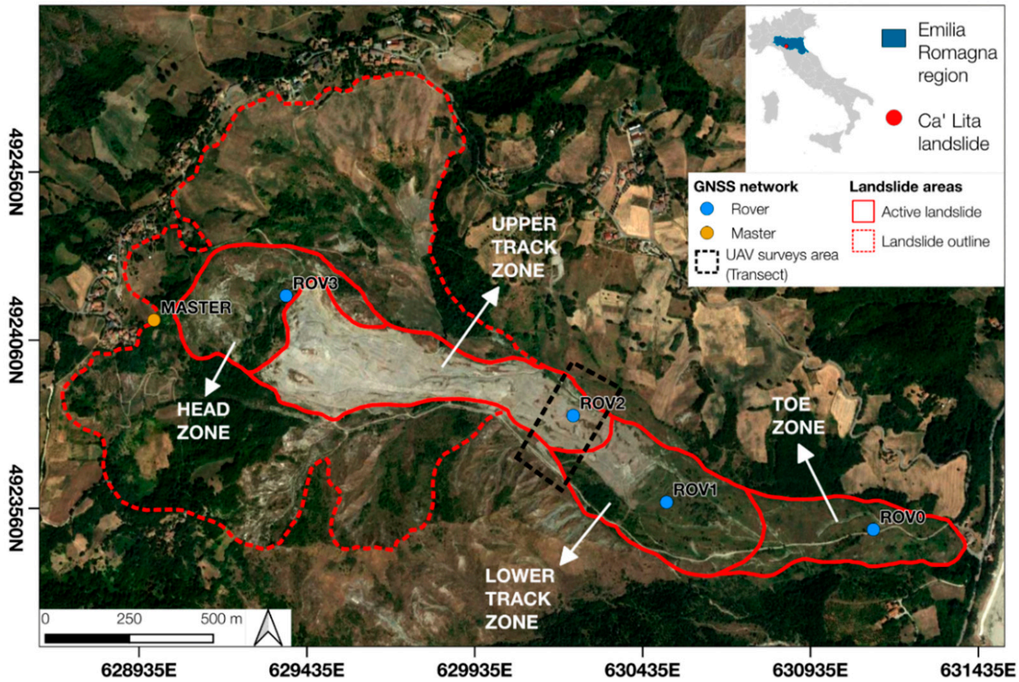

Figure 1. Geographical setting of the Ca' Lita landslide. The black box represents the analyzed transect, while blue and yellow symbols show the GNSS rover and master locations, respectively. The simple red line highlights the distribution of the presently active landslide's body which moves towards the SE (reference system: WGS84 UTM Zone 32N, EPSG: 32632).

A new paroxysmal reactivation of the landslide occurred in March 2016; it caused displacements of tens of meters in the head zone and more than a hundred meters in the track zone [62]. Most of the installed structural mitigation measures were compromised, retaining walls were partly overthrown or damaged and part of the deep-drainage wells were no longer functional [62]. To support civil protection works, a GNSS monitoring system was implemented starting from 24 March 2016 until June 2016 (Figure 1), and it was composed of three rover units and one reference master unit [62,63].

By the end of April 2016, the upper part of the earthslide–earthflow showed 44 m of cumulated planimetric displacement, while in the lower part, 2.7 m was reached. The head zone, however, was not affected by significant movements.

From May to June 2019, another paroxysmal reactivation occurred where, in a period of only 12 h, 9.6 m planar and −2 m vertical displacement were reached along the head zone. Due to downslope movement propagation, 70 m planimetric displacement in the upper track zone and 40 m in the lower track zone were recorded [55]. By the end of November 2019, a new rover unit was added to the GNSS monitoring system and located in the toe zone [62]. After almost two years of inactivity, two other major reactivations occurred in May 2022 and May 2023, each lasting for several months. New GNSS data concerning these events will be presented in detail in Sections 3.4 and 4.4.

3. Materials and Methods

Our approach involved four phases of work (Figure 2). The first phase focused on conducting multi-temporal UAV surveys over a test area within the landslide. The second consisted of processing the photographs acquired during the UAV surveys using SfM software Agisoft Metashape (version 1.8.4.) to generate orthomosaics and Digital Surface Models (DSMs). In the third, within a Geographic Information System (GIS) environment

(QGIS.org (2023), QGIS Geographic Information System. Open-Source Geospatial Foundation Project, http://qgis.org, accessed on 5 December 2023), visual tracking was carried out on *ground* and *reference targets* installed in the test area for each survey. The tracking method consisted of manually placing a point in correspondence with the center of the targets and calculating their differential movement by comparing each survey. This method led to the identification of planimetric and vertical displacements as well as the positioning errors on the *reference target*. Finally, a validation of the obtained planimetric and vertical displacements was conducted by comparing them to displacement values retrieved from GNSS monitoring (see Section 4.4 for more information).

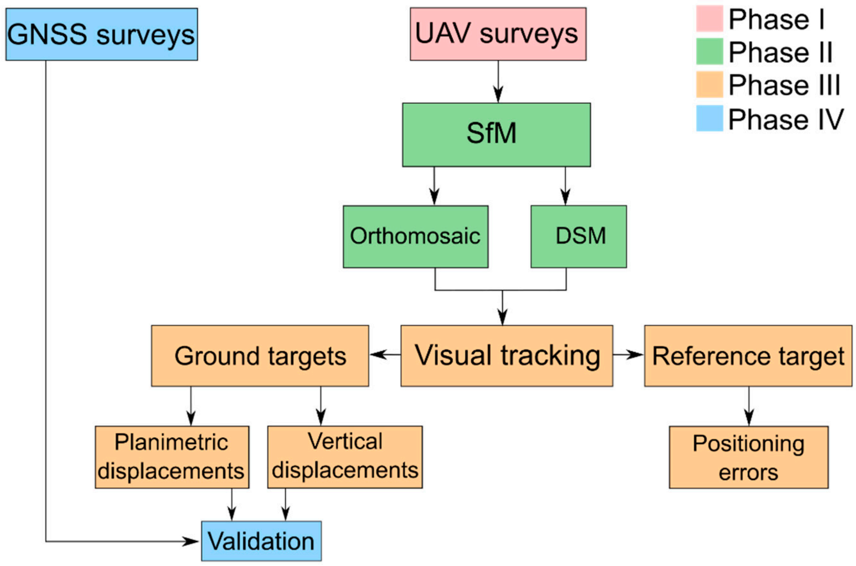

Figure 2. Schematic model representing the four phases of the workflow, highlighted with different colors.

3.1. UAV Monitoring

The multi-temporal aerial surveys were conducted using a DJI Phantom 4 RTK manufactured by DJI Hong-Kong (Figure 3A), classified as a micro drone with a weight of 1.391 kg and 35 cm width [64], equipped with a GNSS positioning system able to receive RTK corrections. At a known ground control point outside of the landslide area, an external double-frequency GNSS receiver casting RTK corrections (*DJI D-RTK 2 Mobile Station manufactured by DJI Hong-Kong*) (Figure 3B) was placed, always at the same point with known coordinates for each survey, and acted as the base station.

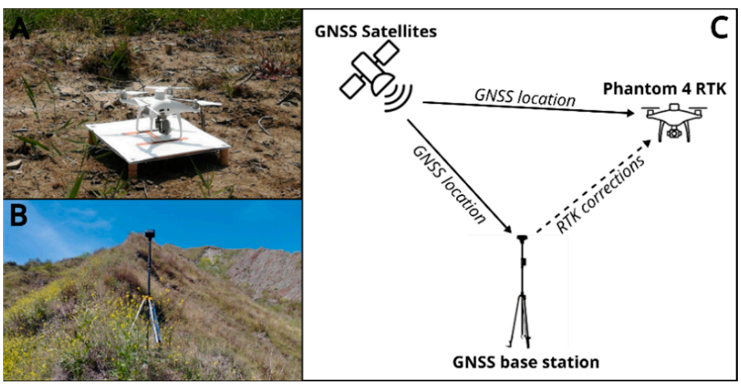

Figure 3. Components of the aerial survey. (**A**) Quadcopter with RTK-receiving module (*DJI Phantom 4 RTK*); (**B**) GNSS base station with RTK-transmitting module (*DJI D-RTK 2*). (**C**) Simplified concept of the correction strategy for RTK solution.

During flight, the drone can directly geocode each acquired photogram with the RTK-corrected coordinates. It avoids the post-processing step or canonical GCP placement and GNSS survey that is required when acquiring data without the RTK module (Figure 3C).

From October 2020 to March 2023, a total of 8 UAV surveys were carried out (Table 1) with an increased frequency following the reactivations of the landslide in May 2022 and March 2023. The surveys were conducted over an area of approximately 60,000 m^2 located in the upper track zone of the landslide. This area represents the portion of the landslide that experienced the most significant displacements during the previous reactivations, making it the ideal place for testing such a rapid monitoring technique.

Table 1. List of the 8 UAV surveys conducted from October 2020 to March 2023 over the investigated transect.

UAV Surveys	
Survey	**Date (YYYY/MM/DD)**
I	2020/10/21
II	2022/05/13
III	2022/05/19
IV	2022/06/17
V	2022/07/13
VI	2023/01/03
VII	2023/03/13
VIII	2023/03/21

A flight plan was prepared and downloaded on the UAV controller before the aerial operations were started, and it was used in all the flights conducted. The flight parameters were chosen to strike a balance, aiming for good image quality and resolution while limiting flight and frame processing times. Therefore, an altitude of 37 m above ground level was selected to achieve a Ground Sample Distance (GSD) of 1.01 cm/px, a resolution that allows for the accurate identification of the targets. The flight speed was set at 2.9 m/s, resulting in a flight time of approximately 17 min. The number of captured photos is 415, a quantity that ensures acceptable processing times using a moderately priced machine. All the flight parameters used are listed in Table 2.

Table 2. List of values selected for each flight parameter.

UAV Flight Parameters	
Altitude above ground	37 m
Speed (m/s)	2.9 m/s
Ground Sampling Distance (GSD)	1.01 cm/px
Image forward overlap	70%
Image side overlap	80%
Gimble angle	−90°
RTK status	Fixed
Flight time	17 min 9 s
Number of photos	415
UAV weight	1.391 kg
UAV size	350 mm

The frames captured were processed using Agisoft Metashape, SfM software, to generate a DSM and an orthomosaic for each conducted survey. The software was installed on a computer with an Intel Core i7-10700Il CPU, 16 GB of RAM and an NVIDIA T-1000/896 CUDA Core GPU.

The processing of the frames involved several steps: (i) image input, (ii) photo alignment, (iii) dense cloud building, (iv) DSM building, (v) orthomosaic building.

During the selection of parameters to be used in the various processing steps of the software, an attempt was made to find a balance between the precision and resolution of the final products and processing times. For photo alignment and dense cloud building, medium accuracy settings (resulting in a processing time of 4 min) and medium quality settings (processing time of 27 min) were used, respectively. For DSM and orthomosaic building, resolutions of 0.03 m (processing time of 1 min) and 0.009 m (processing time of 14 min) were set instead.

Within the test area, 8 targets were installed transversally to the main displacement direction of the landslide and equally spaced to optimally cover the transect and to detect NW–SE movements (Figure 4). Landslide movement in the track zone takes place over multiple sliding surfaces, the deeper one ranging from approximately 10 m to almost 30 m depth [53,54]. Each target consisted of a 50 cm × 50 cm metal white and red-colored panel anchored to the ground by using 2.5 m long steel poles equipped with a helical tip driven 1.5 m into the ground (Figure 5A). Given the high magnitude and the prevalent translation pattern of monitored movements, the displacement of a target is without doubt attributed to the general landslide movement rather than local effects, which are considered substantially negligible. Out of the 8 targets, 7 were installed inside the landslide area (P_02, P_03, P_04, P_05, P_06, P_07 and P_08), and 1 (P_01) was installed outside the landslide area, on stable bedrock, near the GNSS base station, so to consider it a reference target (Figure 5C,E). Moreover, a *ground target* (P_05) was installed at approximately 4 m from ROV_2 (Figure 5D), a GNSS rover belonging to the GNSS monitoring network (Figure 5B). This configuration allowed us to compare the displacements of the target, measured between successive surveys, with displacements recorded by the GNSS rover. This was done to validate the rapid assessment of landslide dynamics using UAV-RTK. In fact, the goal of the present study is to determine the planimetric and vertical displacements of the *ground targets* together with the quantification of errors, conducted on the *reference target*, between successive UAV surveys.

Figure 4. Panoramic of the studied transect with the distribution of the 8 *ground targets*, the RTK base station in yellow and GNSS ROV2 in blue (reference system: WGS84 UTM Zone 32N, EPSG: 32632).

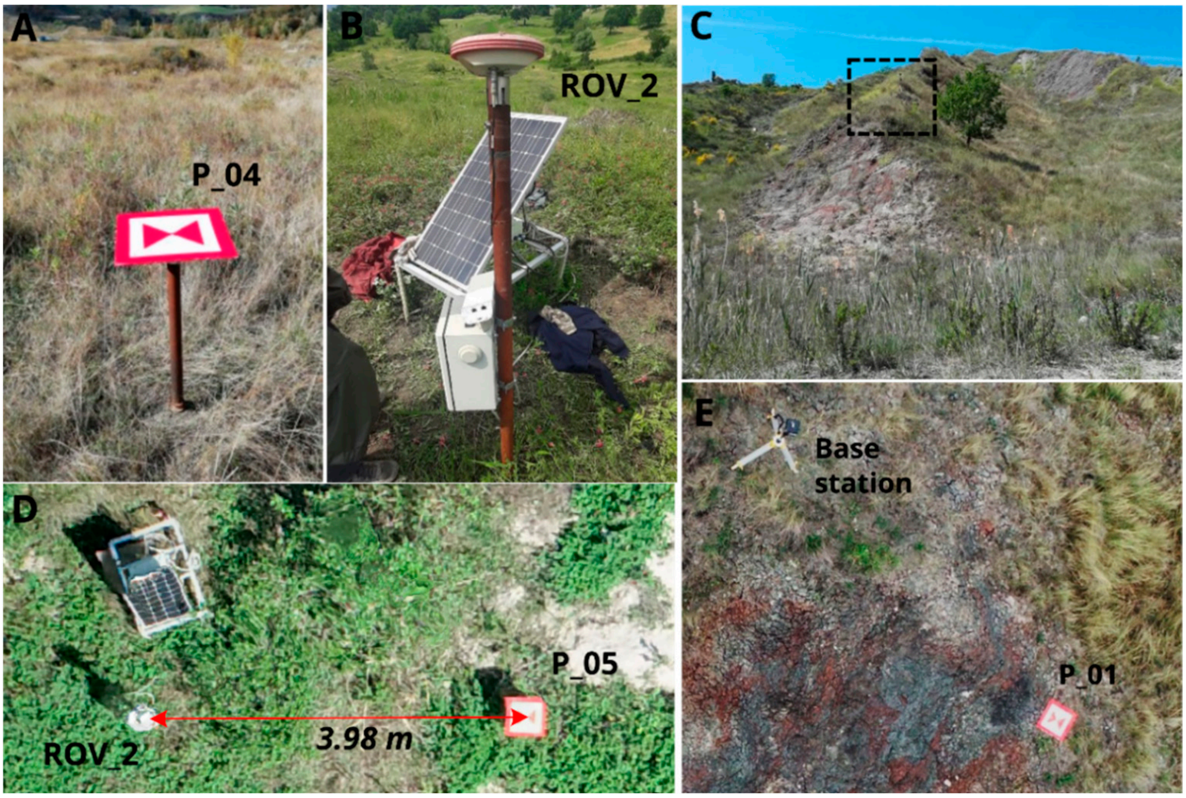

Figure 5. Installed instrumentations. (**A**) P_04 *ground target*; (**B**) ROV2 connected with a solar panel for alimentation; (**C**) overview of the bedrock crest where the base station and the *reference target* (P_01) were placed; (**D**) planimetric distance between ROV2 and P_05; (**E**) zoom in on the base station and P_01.

3.2. Target Visual Tracking

Orthomosaics and DSMs were analyzed in a GIS environment to calculate the planimetric and vertical displacements of the *ground targets* and assess the survey precision by checking the *reference target* positioning bias. As already outlined in Figure 1, once the targets were visually identified on each orthomosaic, their coordinates were recorded and visual tracking was performed, allowing for the determination of their planimetric displacements. Vertical displacements, on the other hand, were calculated by extracting the target elevation from the DSM in correspondence with the point at the center of the target and then computing the difference with the elevation extracted for the same target from the DSM of the subsequent survey. Finally, to determine the positioning errors of the *reference target*, its position and elevation acquired during each survey were compared in pairs with the identified positions and elevations in all the other surveys.

3.3. Continuous GNSS Monitoring

A GNSS array has been installed in the landslide since the end of March 2016 [62]. The dataset presented in this contribution is derived from an array composed of two master stations and four rover receivers (Figure 1). Receivers ROV3, ROV2 and ROV1, together with their master station, are part of an array of receivers all composed of LEICA instruments. More precisely, at the master station, a double-frequency “Leica GMX902” receiver is installed, while all the rover receivers of this “Leica array” are single-frequency “smart antennas Leica GMX901” receivers. On the other hand, rover ROV0 and its master station, installed in the same area as the Leica master station, are low-cost single-frequency receivers branded “Emlid Reach RS+”. All the rover stations are energy-independent since they are powered by photovoltaic panels, while master stations are connected to the 220 V AC grid.

Hourly solutions are sent and stored by both systems to a remote server located in the University facility. The Leica array uses the Leica Spider software (version 7.9.0.) to compute hourly double-difference coordinate solutions for each rover with respect to the Leica master station. The Emlid low-cost array sends one-hour-long packets of RTK coordinate solutions sampled at 5 Hz to the University server. Then, hourly mean coordinates are computed and stored to generate displacement time series. All rovers' GNSS displacement time series are hourly data that are resampled daily and, for battery-saving policy, are acquired only during the daytime.

3.4. Methods for Error Estimation and Result Validation

As with any other method, rapid surveys are affected by multiple sources of errors: (i) A first source of error is related to the accuracy in georeferencing the surveys, and this is generally minimized by using GCPs (i.e., by GNSS survey of targets). However, in this application, the use of GCPs has been discarded to test a much more rapid and versatile method for assessing slope movements. (ii) A second source of random errors is related to the procedure of target tracking, i.e., the visual identification of the center of the target, which is affected by pixel size and by human factors. An estimate of the sum of these positioning errors can be obtained by considering the scattering of the *reference target* (P_01) positions in time, since such a *ground target* is installed on solid bedrock outside the landslide area, and its stability over time is practically certain. So, the median value of its planimetric displacements and relative vertical displacements will be considered as the positioning error. Furthermore, to validate the displacement estimate results, a comparison can be carried out between the displacement time series of the permanent GNSS (ROV_2) and that of the nearest *ground target* (P_05), installed at 3,98 m distance. This approach of validation is considered acceptable under the assumption that the landslide will locally move as a slide, i.e., that displacement rates on the surface are the same over such short distances.

4. Results and Discussion

4.1. Ground-Target Displacements

The values of cumulative planimetric and vertical displacements are summarized in Table 3, while targets' coordinates are presented in Appendix A. Both cumulative planimetric and vertical displacements of each survey are calculated as the displacement occurred with respect to the first survey (I).

Table 3. Summary of the planimetric cumulative displacements (Cum. Displ.) and vertical displacements (ΔH) estimated for each survey.

Surveys	P_01		P_02		P_03		P_04		P_05		P_06		P_07		P_08	
	Cum. Displ.	ΔH	Cum. Displ.	ΔH	Cum. Displ.	ΔH	Cum. Displ.	ΔH	Cum. Displ.	ΔH	Cum. Displ.	ΔH	Cum. Displ.	ΔH	Cum. Displ.	ΔH
I	0.00	0.00	0.00	0.00	0.00	0.00	0.00	0.00	0.00	0.00	0.00	0.00	0.00	0.00	0.00	0.00
II	0.004	0.00	0.02	0.01	4.61	0.41	4.08	0.05	4.22	0.34	0.00	−0.11	0.39	−0.08	0.01	−0.03
III	0.007	−0.03	0.02	−0.03	8.75	0.86	8.01	0.06	8.35	0.69	0.59	−0.24	0.74	−0.16	0.00	0.01
IV	0.022	−0.03	0.01	−0.03	15.56	1.63	14.50	0.16	15.34	1.31	1.13	−0.50	1.40	−0.34	0.02	0.02
V	0.003	−0.02	0.03	−0.02	16.37	1.76	15.27	0.19	16.15	1.38	2.01	−0.53	1.52	−0.37	0.00	0.03
VI	0.002	−0.03	0.06	0.04	19.97	2.28	18.65	0.68	19.67	1.55	2.17	−0.72	2.06	−0.55	0.01	−0.04
VII	0.008	−0.06	0.09	0.01	51.52	4.83	52.45	3.80	53.03	3.73	2.81	−1.80	7.32	−1.77	0.01	−0.02
VIII	0.014	−0.08	0.10	0.00	68.32	5.94	66.40	4.62	71.61	4.46	9.74	−2.04	9.01	−2.05	0.00	0.05

Values are expressed in meters.

Looking at the results, a clear distinction can be recognized between the essentially stable *reference target* (P_01) and the other *ground targets*. Differences are distinguishable also in Figure 6A showing the targets' positions for each survey and in Figure 6B,C where the related planimetric and vertical displacement path is presented.

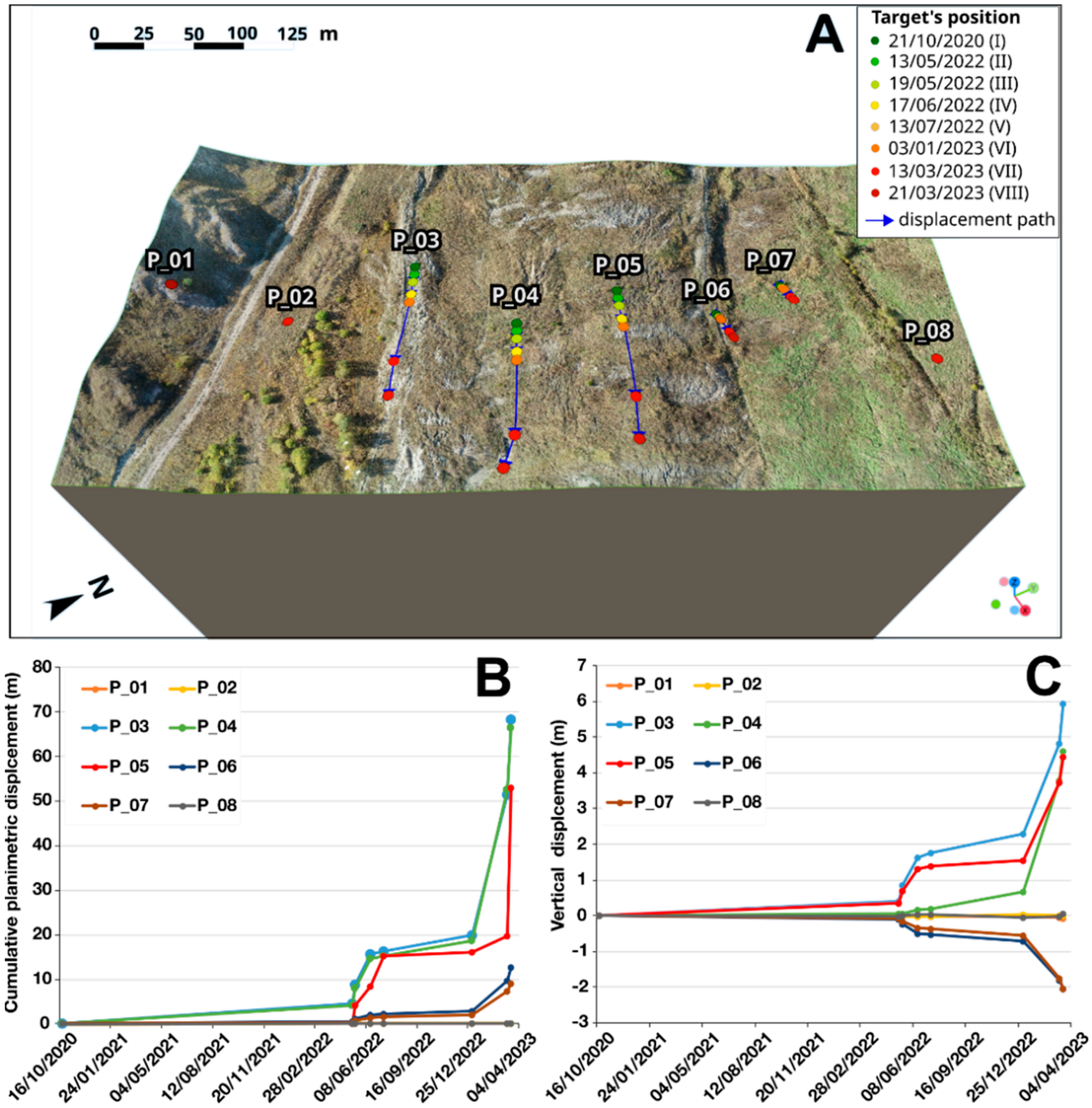

Figure 6. Results of the visual tracking of targets. (**A**) Colored points represent the positions of each target from the first UAV survey (dark green) until the last one (dark red); (**B**) cumulative planimetric displacement; (**C**) vertical relative displacement (reference system: WGS84 UTM Zone 32N, EPSG: 32632).

The visual tracking of *ground targets* (Figure 6A) from orthomosaics and DSM highlighted significant planimetric and vertical displacements (Figure 6B,C). The largest planimetric displacements were measured by targets P_03, P_04 and P_05 (Figure 7C–E) located along the central axis of the flow, while, moving towards the lateral areas, the measured displacements significantly decrease (P_06 and P_07 in Figure 7F,G) until the edges of the landslide body; see P_02 (Figure 7B). Lastly, P_08 can be considered as stable (Figure 7H).

As observed from both Table 3 and Figure 6B,C, the largest relative planimetric displacements of the ground targets were measured between the sixth survey (3 January 2023—VI) and the seventh survey (13 March 2023—VII). In the central zone, target P_03 showed a displacement of 31.580 m, while targets P_04 and P_05 recorded displacements of 33.799 m and 33.301 m, respectively. Targets P_06 and P_07, in the lateral zone, showed planimetric displacements of 1.083 m and 2.403 m, respectively. Likewise, the largest relative vertical displacements were recorded between 3 January 2023 (VI) and 13 March 2023 (VII). The cumulative planimetric displacement values measured throughout the entire observed period range from 9.01 m (P_07) to 71.61 m (P_05).

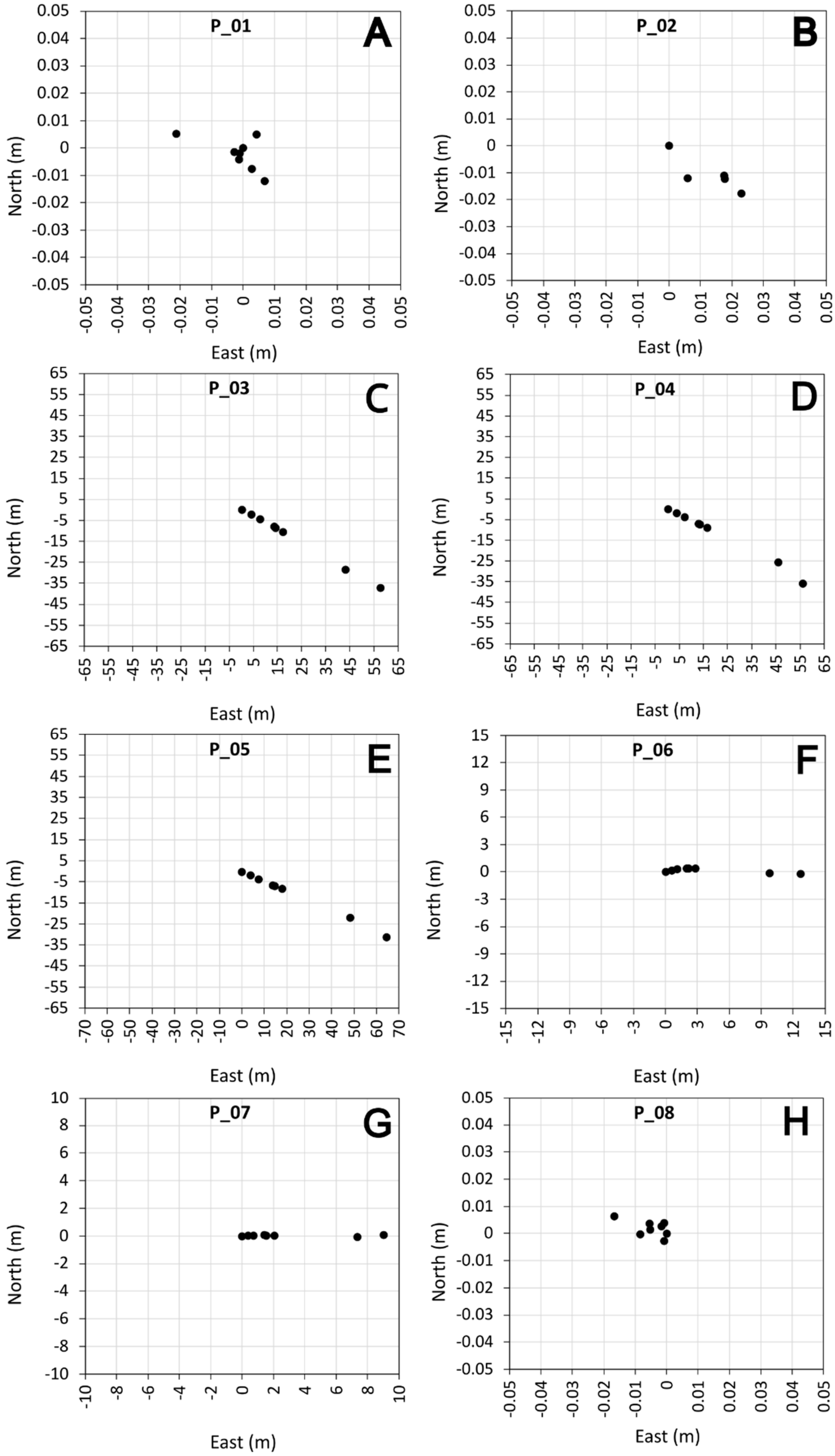

Figure 7. Scatter plots representing the relative displacement with respect to the first survey of each target within the N-E plane. (**A**) *reference target*; (**B**,**H**) most external *ground targets*; (**C**–**G**) central and later *ground targets*.

4.2. Detecting Landslides' Dynamics

As previously stated, the test area chosen for the application of this rapid monitoring method was a 60,000 m^2 transect located within the upper track zone of the Ca' Lita landslide. In detail, the dimension of the area covered by aerial surveys is approximately 350 m orthogonally and 190 m along the downslope movement direction. The width of the landslide's body in this part ranges between 220 and 297 m, and as for the kinematic aspect, the area is classified as predominantly earthflow–earthslide [53,54]. Where lateral margins or surfaces of rupture are clearly distinguishable, the predominant process could be sliding, while it is highly probable that when the moving mass is internally deformed and follows a distribution of velocities typical of viscous liquid, the predominant process is flowing [65]. In the present case study, the analyzed transect shows both kinematic styles.

As we can observe in Figure 8, *ground targets* can be divided into two groups based on their velocities, leading to a delimitation of faster and slower portions of the landslide. P_03, P_04 and P_05, which are in the central faster part, are characterized by velocities around 50 cm/day, while P_06 and P_07, located in the marginal area, show significantly lower velocities (7–10 cm/day). On the other hand, P_02 shows a clear direction of flow (compatible with the kinematic of the local geomorphic area) but is characterized by a total cumulated planimetric displacement of around 0.1 m. P_08, together with the *reference target*, P_01, could be considered essentially stable with an oscillation of its displacement values that are related to the estimated methodological error proposed before.

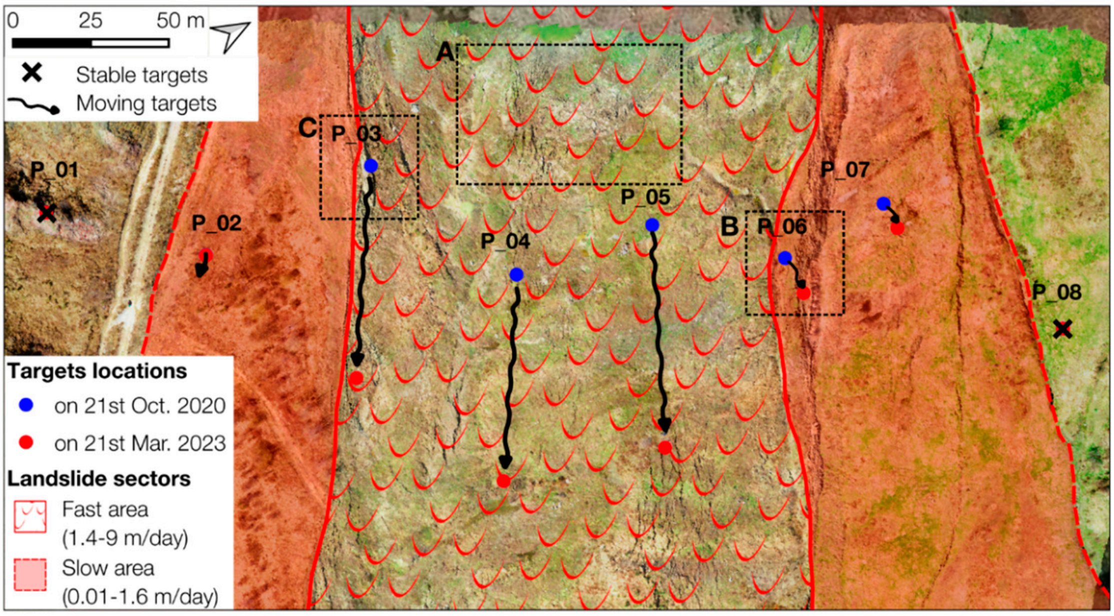

Figure 8. Interpretation of the landslide dynamics in correspondence with the analyzed transect. Initial (blue dots) and final (red dots) targets' locations are displayed. The landslide's body has been subdivided into areas based on the recorded velocities: fast area in the central part and slower areas along the flanks. The three boxes highlighted with A, B, and C in dashed lines show deformation structures that will be described in Figure 9. Base map: 21 March 2023 orthophoto and hillshade. (Coordinates: top left 630,065.87E, 4,923,689.51N, bottom right 630,407.53E, 4,923,906.02N; reference system: WGS84 UTM Zone 32N, EPSG: 32632).

The overall distribution of displacements along the investigated transect can be compared to that of a viscous liquid channelized in the track zone that, as previously said, together with areas of significant internal deformation (Figure 9A), constitutes a fundamental characteristic of earthflows. Moreover, looking at the flanks of the landslide's body (Figure 9B,C), although numerous fractures are visible, one main surface of rupture can be traced along all the transect, thus confirming the combination of earthflow and earthslide types of movement that was already proposed in previous works [53,54,66].

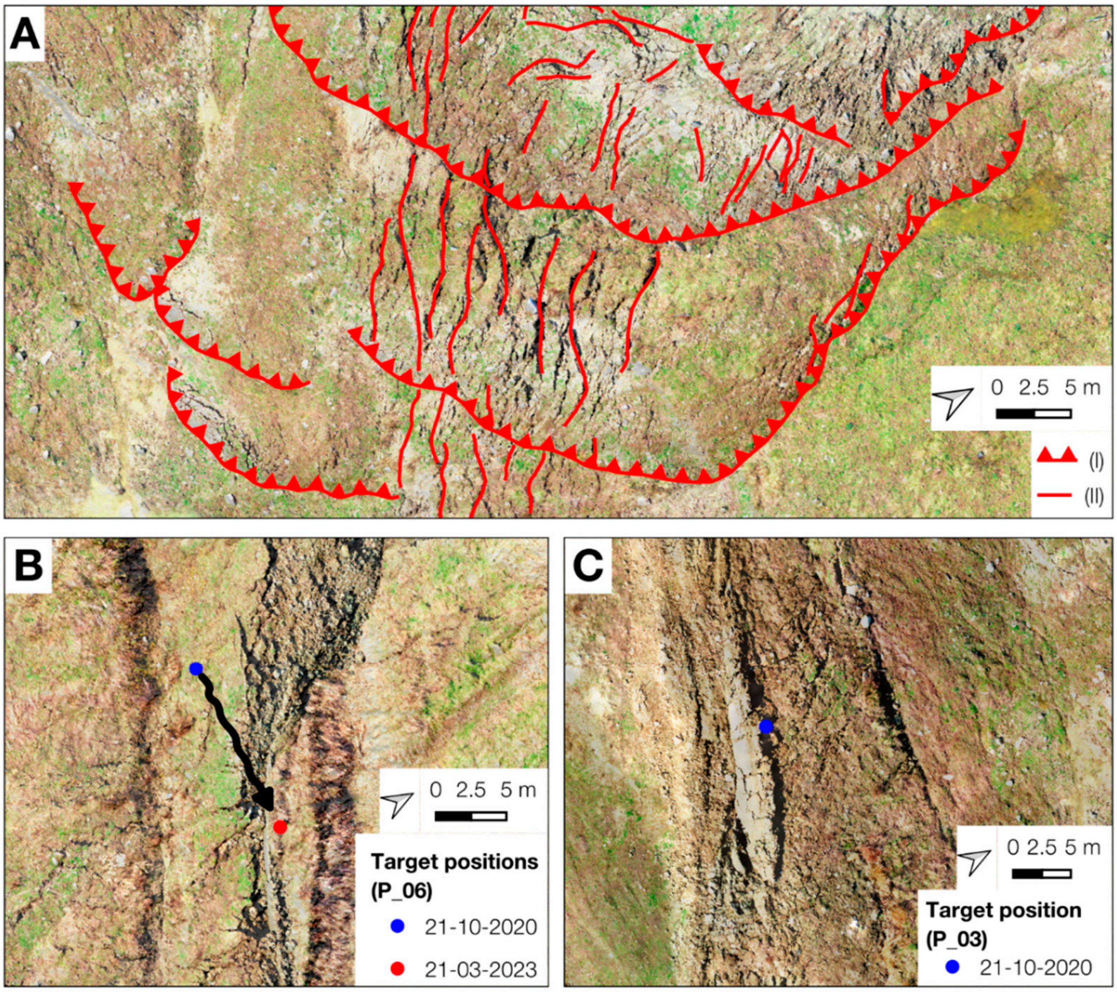

Figure 9. Detailed areas of the analyzed transect presented in Figure 8 (highlighted in dashed boxes). (**A**) Compressional structures located in the central part of the flow are highlighted in red: (I) thrust, (II) fracture. (**B**,**C**) Lateral areas of the landslide, right and left, respectively, where surfaces of rupture are clearly visible. Like in Figure 8, blue and red points represent targets' locations. In (**C**), the red point (P_03) is out of the zoomed box. Base map: 21st March 2023 orthophoto and hillshade (reference system: WGS84 UTM Zone 32N, EPSG: 32632).

4.3. GNSS Displacements

As mentioned in Section 2, after June 2019, Ca' Lita underwent a stable period of 2 years with no acceleration event. Then, two major reactivations took place around May 2022 and March 2023. In detail, during the first event, in the head zone (ROV3), 13 m of planimetric and ≈2.6 m of vertical displacement were reached, while in the upper track zone (ROV2) and in the lower track zone (ROV1), 12 m and 1.6 m were reached, respectively. During the second event, the head zone (ROV3) showed 6.5 m of planimetric and 1 m of vertical displacement, and the upper track zone (ROV2) reached 50 m of displacement. ROV1, in the lower track zone, was temporarily out of service, while at the foot (ROV0), for the first time, 2.2 m of planimetric displacement and 0.4 m of vertical displacement were recorded. Planimetric and vertical displacements related to both reactivations are shown in Figure 10.

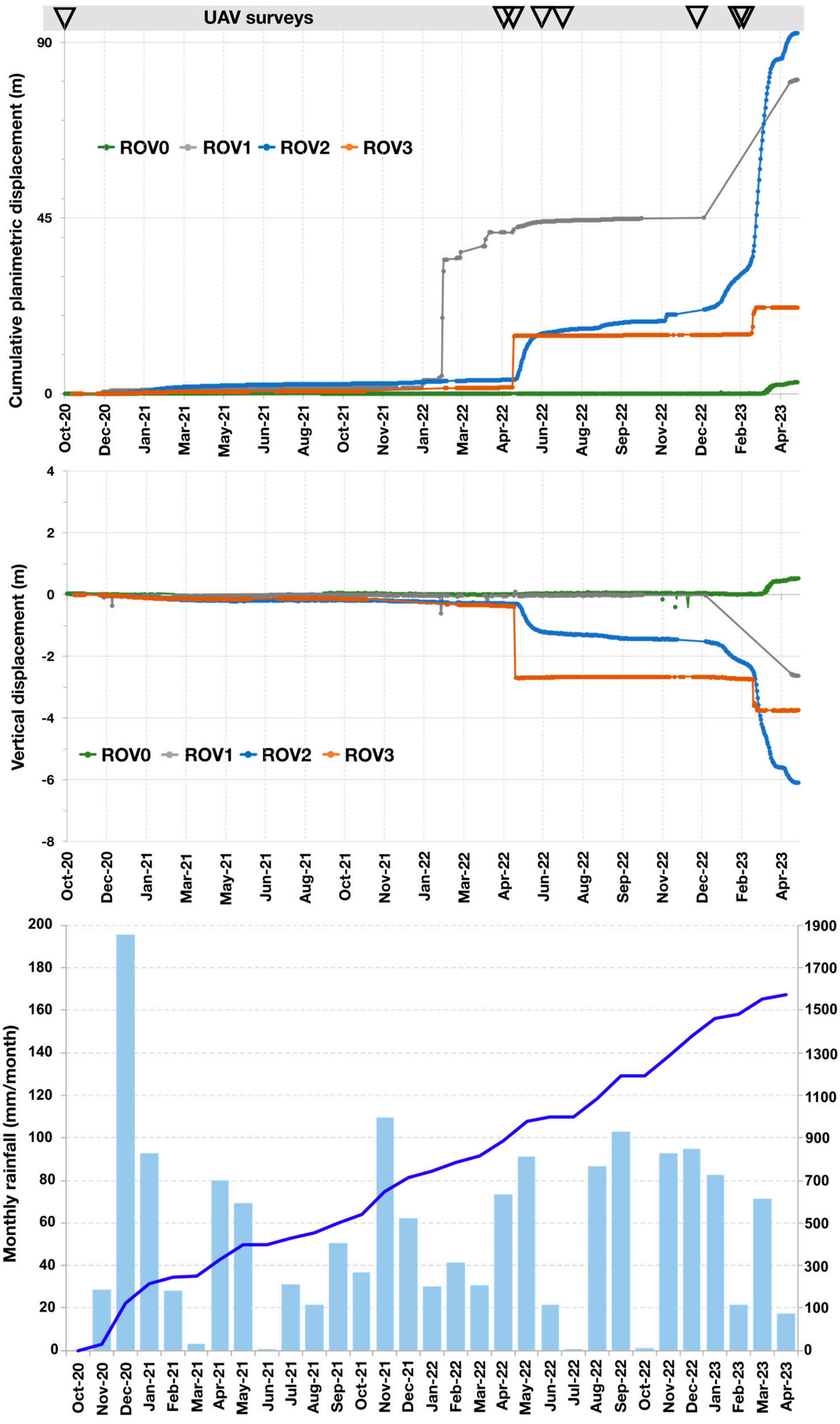

Figure 10. In the upper part: cumulative planimetric and vertical displacements of the four continuous GNSS during the last three years; UAV surveys covering the period that has been studied are highlighted with black triangles. In the lower part: monthly rainfall (mm/month) with the cumulated line in blue; precipitation data are taken from Baiso Station (Arpae network) covering the studied period from 30 October 2020 to 30 April 2023.

Looking at the precipitation plot (Figure 10), no significant and direct relationship was found between landslide accelerations and monthly precipitation patterns. Although rainfall certainly has an important role in triggering instabilities, in this case, it cannot be considered the only driving factor. The discrepancy between rainfall and acceleration can be observed when comparing December 2020 rainfall (almost 200 mm in a month) that did not lead to an acceleration to March–April 2022 rainfall (around 100 mm in 2 months) when a major reactivation took place.

On the other hand, considering the complexity of Ca' Lita, the overall mechanical equilibrium of stresses within the landslide's body represents a fundamental aspect of instability. In particular, the dynamics of the studied transect, which corresponds to the upper track zone, is mechanically connected to the depletion of material that falls from the head zone on top of the earthslide–earthflow below causing internal undrained stresses that propagate along the landslide's body. However, as already stated before, precipitation still plays an important role in landslides' instabilities, as was the case for the last major reactivation that took place in May 2023. Intense rainfall occurred in the first half of May 2023 which led to displacements of hundreds of meters. They caused a complete change in the morphology of the whole landslide and damaged three out of four continuous GNSS stations (ROV0, ROV1 and ROV2), as well as causing the extirpation of the ground targets previously installed for the present study. Having said that, we left the last reactivation out of our analysis as it goes beyond the main purposes of this study.

4.4. Error Estimation and Result Validation

Considering P_01 a stable target for its chosen geological location (reference target), the median of its vertical and planimetric values across all surveys revealed 0.01 and 0.03 m methodological positioning errors for the horizontal and vertical components (Table 3 and Figure 7A).

To proceed with the validation of results obtained following this approach of rapid assessment, which represents the fourth and last phase of this study, a comparison between data from the *ground target* P_05 and GNSS measurements recorded by ROV_2 was carried out.

Looking at Table 4, it can be seen that cumulative planimetric and vertical displacements for both P_05 and ROV_2 are very similar, essentially in the order of 1×10^{-2} m.

Table 4. Summary of cumulative planimetric and vertical displacements together with absolute offset between the *ground target* P_05 and ROV2 belonging to the GNSS network [$|\Delta|$ (P_05 − ROV_2)].

Surveys	P_05		ROV_2		$|\Delta|$ (P_05 − ROV_2)	
	Cum. Displ.	ΔH	Cum. Displ.	ΔH	Cum. Displ.	ΔH
I	0.00	0.00	0.00	0.00	0.00	0.00
II	4.22	0.34	4.26	0.33	0.046	0.003
III	8.35	0.69	8.43	0.64	0.082	0.046
IV	15.34	1.31	15.43	1.21	0.093	0.097
V	16.15	1.38	16.23	1.28	0.086	0.102
VI	19.67	1.55	19.74	1.51	0.077	0.039
VII	53.03	3.73	53.04	3.91	0.013	0.184
VIII	71.61	4.46	71.43	4.67	0.178	0.208

Values are expressed in meters.

Despite these discrepancies and considering that the order of planimetric displacement of this area is tens of meters, the general trend of displacement is the same for P_05 and ROV_2 in the vertical and horizontal components (Figure 11A,B).

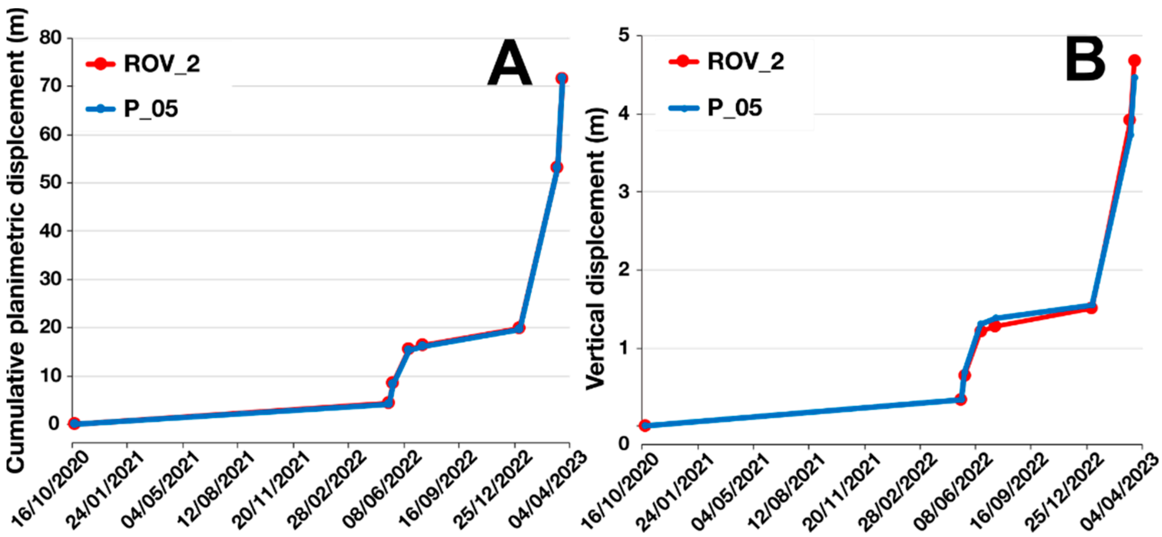

Figure 11. Plots showing the comparison of (**A**) cumulative planimetric displacement (m) and (**B**) vertical displacement (m) for ROV_2 and P_05 from October 2020 to April 2023.

5. Conclusions

Having chosen to present a rapid method for assessing landslide dynamics occurring within an active landslide, the main objective of this work was that of finding the fastest combination between data acquisition, processing and analysis with the highest precision possible. We estimated that the proposed workflow (Figure 2), which was applied in this study, takes around 70–75 min to complete. In detail, each of the three phases is characterized as follows: (i) 17 min for UAV surveys, (ii) 45 min for elaboration with SfM software (Agisoft Metashape), (iii) 10–15 min for the visual tracking of targets. Considering the errors that are inevitably introduced in this analysis due to the georeferencing process as well as human decisions in the visual tracking part, the accuracy and precision achieved with this monitoring system (0.01 m planimetric and 0.03 m vertical) are more than enough to assess earthflow dynamics. Moreover, the rapidness that characterizes this application makes it possible to follow the evolution of the landslide day by day, especially during periods of alertness.

The results obtained in this study about the application of a rapid UAV-RTK method on earthflows–earthslides showed that it was possible to achieve sufficient accuracy and precision without implementing ground control points. A significant limitation of using GCPs is the longer acquisition times, while the aim was, in fact, that of finding a fast and repeatable way of monitoring such phenomena characterized by periodically abrupt evolutions. The necessity of having, at least, a day-by-day result to follow emergency situations as much as possible was put as a top priority. The Ca’ Lita landslide, in the Reggio Emilia province, was the ideal example for testing this approach, which briefly consists of performing multi-temporal UAV surveys using a combination of a DJI Phantom 4 RTK and an external D-RTK 2 mobile station. The proposed workflow, from UAV surveys to visual tracking, takes at most 70–75 min.

The potential sources of errors, random and systematic, estimated by considering the scattering of the *reference target* (P_01, Figure 7A) positions in time and by comparing P_05 values with those of the GNSS ROV2 (Figure 11A,B), resulted in a maximum planimetric positioning error of 2.5 cm and a maximum vertical positioning error of 3.2 cm. Unlike what happens in other applications, such as those related to cultural heritage management where even millimeter precision is needed [67], in this context (considering the landslide activity), centimetric planimetric and vertical errors can be considered as acceptable. The major scattering (22.3 cm vertical and 18.6 cm planimetric displacement) is encountered during the period 3 January 2023–21 March 2023, in correspondence with the main acceleration.

Considering the landslide's kinematics, this behavior could be attributed to a lifting due to a vertical bulge and then a tilt forward of the target pole.

In conclusion, by analyzing data obtained from the elaboration of UAV surveys (i.e., orthophotos and hillshades) together with the *ground-target* visual tracking technique, we could (i) discriminate between faster and slower areas within the transect itself, the velocities of which appear to be distributed as a typical viscous fluid (Figure 8), and (ii) highlight in greater detail superficial morphologies resulting from the combination of flowing (Figure 9A) and sliding (Figure 9B,C).

Implementing small UAV procedures for monitoring landslides, especially large-scale ones, has again proved its advantages, among which the rapidity of repeated surveys and the possibility of having a safely complete overview of the landslide area are certainly the most appreciated.

In particular, the tested methodology proved to be a reliable technique in terms of rapidity, precision and repeatability as well as a low-cost useful tool for the interpretation and description of the phenomenon, being of significant added value for detecting and assessing earthflow–earthslide dynamics on a day-by-day basis.

Author Contributions: Research design: G.C., A.C. and M.M.; data processing and analysis: G.C., M.T., M.M. and A.C.; result analysis and discussion: G.C., M.T., M.M., G.B. and A.C.; manuscript preparation (text, figures and tables): G.C., M.T., M.M. and A.C.; internal review and editing: G.C., M.T., M.M., G.B. and A.C. All authors have read and agreed to the published version of the manuscript.

Funding: The PhD grant of M.T. is funded by the European Regional Development Fund (PON 2014–2020—Research and Innovation, in actuation of DM1061/2021). The research is part of "CC-SLOPE" project, funded by the European Regional Development Fund (PON 2014–2020 Research and Innovation, in actuation of DM1062/2021). The research has also been supported by the Regional Agency for Territorial Security and Civil Protection of Emilia-Romagna (Research collaboration and scientific and informative technical activity for hydrogeological risk prediction, prevention, and management) and the University of Modena and Reggio Emilia (FAR2023 Department of Chemical and Geological Sciences).

Data Availability Statement: The data presented in this study are owned by the University of Modena and Reggio Emilia and are not available publicly.

Conflicts of Interest: The authors declare no conflicts of interest.

Appendix A

Table A1. Geographical coordinates (E, N and H) of all the targets installed (reference system: WGS84 UTM Zone 32N, EPSG:32632).

Surveys	P_01			P_02			P_03		
	E	N	H	E	N	H	E	N	H
I	630,130.388	4,923,669.228	393.775	630,167.219	4,923,707.446	381.878	630,167.791	4,923,767.687	386.021
II	630,130.386	4,923,669.224	393.770	630,167.236	4,923,707.435	381.890	630,171.830	4,923,765.462	385.613
III	630,130.392	4,923,669.233	393.742	630,167.237	4,923,707.434	381.845	630,175.317	4,923,763.228	385.161
IV	630,130.366	4,923,669.234	393.743	630,167.225	4,923,707.434	381.848	630,181.154	4,923,759.712	384.391
V	630,130.385	4,923,669.227	393.752	630,167.242	4,923,707.428	381.862	630,181.840	4,923,759.277	384.260
VI	630,130.387	4,923,669.226	393.749	630,167.272	4,923,707.410	381.918	630,184.824	4,923,757.271	383.739
VII	630,130.390	4,923,669.221	393.717	630,167.299	4,923,707.405	381.890	630,210.669	4,923,739.122	381.191
VIII	630,130.394	4,923,669.216	393.699	630,167.306	4,923,707.406	381.880	630,225.157	4,923,730.578	380.086

Table A1. *Cont.*

Surveys	P_04			P_05			P_06		
	E	N	H	E	N	H	E	N	H
I	630,221.011	4,923,791.641	381.824	630,228.221	4,923,837.489	386,412	630,258.181	4,923,869.607	380.921
II	630,224.604	4,923,789.700	381.779	630,232.029	4,923,835.677	386.075	630,258.745	4,923,869.779	381.034
III	630,228.059	4,923,787.838	381.766	630,235.780	4,923,833.941	385.722	630,259.270	4,923,869.925	381.165
IV	630,233.779	4,923,784.761	381.667	630,242.156	4,923,831.075	385.106	630,260.150	4,923,870.013	381.419
V	630,234.455	4,923,784.410	381.638	630,242.897	4,923,830.758	385.035	630,260.315	4,923,870.014	381.447
VI	630,237.429	4,923,782.794	381.146	630,246.122	4,923,829.348	384.864	630,260.968	4,923,869.985	381.640
VII	630,266.803	4,923,766.072	378.026	630,276.498	4,923,815.549	382.684	630,267.917	4,923,869.486	382.723
VIII	630,276.962	4,923,755.886	377.206	630,292.735	4,923,806.421	381.95	630,270.872	4,923,869.392	382.960
Surveys	**P_07**			**P_08**			**ROV_2**		
	E	N	H	E	N	H	E	N	H
I	630,258.232	4,923,905.730	380.517	630,321.215	4,923,936.680	381.588	630,224.257	4,923,838.4970	389.4624
II	630,258.625	4,923,905.748	380.601	630,321.207	4,923,936.680	381.621	630,228.090	4,923,836.6310	389.1286
III	630,258.967	4,923,905.775	380.675	630,321.215	4,923,936.682	381.578	630,231.865	4,923,834.8610	388.8185
IV	630,259.632	4,923,905.803	380.859	630,321.199	4,923,936.673	381.565	630,238.250	4,923,831.9900	388.2529
V	630,259.754	4,923,905.781	380.883	630,321.215	4,923,936.675	381.556	630,238.984	4,923,831.6731	388.1872
VI	630,260.289	4,923,905.757	381.065	630,321.210	4,923,936.676	381.631	630,242.205	4,923,830.2735	387.9538
VII	630,265.555	4,923,905.693	382.287	630,321.210	4,923,936.678	381.609	630,272.642	4,923,816.7628	385.5506
VIII	630,267.240	4,923,905.842	382.567	630,321.214	4,923,936.677	381.536	630,288.691	4,923,807.6730	384.7922

References

1. Turner, D.; Lucieer, A.; de Jong, S.M. Time Series Analysis of Landslide Dynamics Using an Unmanned Aerial Vehicle (UAV). *Remote Sens.* **2015**, *7*, 1736–1757. [CrossRef]
2. Mantovani, M.; Bossi, G.; Dykes, A.P.; Pasuto, A.; Soldati, M.; Devoto, S. Coupling Long-Term GNSS Monitoring and Numerical Modelling of Lateral Spreading for Hazard Assessment Purposes. *Eng. Geol.* **2022**, *296*, 106466. [CrossRef]
3. Palis, E.; Lebourg, T.; Tric, E.; Malet, J.P.; Vidal, M. Long-Term Monitoring of a Large Deep-Seated Landslide (La Clapiere, South-East French Alps): Initial Study. *Landslides* **2017**, *14*, 155–170. [CrossRef]
4. Gullà, G.; Calcaterra, S.; Gambino, P.; Borrelli, L.; Muto, F. Long-Term Measurements Using an Integrated Monitoring Network to Identify Homogeneous Landslide Sectors in a Complex Geo-Environmental Context (Lago, Calabria, Italy). *Landslides* **2018**, *15*, 1503–1521. [CrossRef]
5. Malet, J.-P.; Maquaire, O.; Calais, E. The Use of Global Positioning System Techniques for the Continuous Monitoring of Landslides: Application to the Super-Sauze Earthf Low (Alpes-de-Haute-Provence, France). *Geomorphology* **2002**, *43*, 33–54. [CrossRef]
6. Aguzzoli, A.; Arosio, D.; Mulas, M.; Ciccarese, G.; Bayer, B.; Winkler, G.; Ronchetti, F. Multidisciplinary Non-Invasive Investigations to Develop a Hydrogeological Conceptual Model Supporting Slope Kinematics at Fontana Cornia Landslide, Northern Apennines, Italy. *Environ. Earth Sci.* **2022**, *81*, 471. [CrossRef]
7. Hojat, A.; Arosio, D.; Ivanov, V.I.; Longoni, L.; Papini, M.; Scaioni, M.; Tresoldi, G.; Zanzi, L. Geoelectrical Characterization and Monitoring of Slopes on a Rainfall-Triggered Landslide Simulator. *J. Appl. Geophys.* **2019**, *170*, 103844. [CrossRef]
8. Zhang, Z.; Arosio, D.; Hojat, A.; Zanzi, L. Tomographic Experiments for Defining the 3D Velocity Model of an Unstable Rock Slope to Support Microseismic Event Interpretation. *Geosciences* **2020**, *10*, 327. [CrossRef]
9. Mulas, M.; Marnas, M.; Ciccarese, G.; Corsini, A. Sinusoidal Wave Fit Indexing of Irreversible Displacements for Crackmeters Monitoring of Rockfall Areas: Test at Pietra Di Bismantova (Northern Apennines, Italy). *Landslides* **2020**, *17*, 231–240. [CrossRef]
10. Agostini, A.; Tofani, V.; Nolesini, T.; Gigli, G.; Tanteri, L.; Rosi, A.; Cardellini, S.; Casagli, N. A New Appraisal of the Ancona Landslide Based on Geotechnical Investigations and Stability Modelling. *Q. J. Eng. Geol. Hydrogeol.* **2014**, *47*, 29–44. [CrossRef]
11. Azmoon, B.; Biniyaz, A.; Liu, Z. Use of High-Resolution Multi-Temporal DEM Data for Landslide Detection. *Geoscience* **2022**, *12*, 378. [CrossRef]
12. Ghirotti, M.; Donati, D.; Stead, D. Editorial: Developments of Remote Sensing and Numerical Modeling Applications for Landslide Analysis. *Front. Earth Sci.* **2023**, *10*, 1129733. [CrossRef]
13. Dematteis, N.; Wrzesniak, A.; Allasia, P.; Bertolo, D.; Giordan, D. Integration of Robotic Total Station and Digital Image Correlation to Assess the Three-Dimensional Surface Kinematics of a Landslide. *Eng. Geol.* **2022**, *303*, 106655. [CrossRef]
14. Corsini, A.; Bonacini, F.; Mulas, M.; Petitta, M.; Ronchetti, F.; Truffelli, G. Long-Term Continuous Monitoring of a Deep-Seated Compound Rock Slide in the Northern Apennines (Italy). *Eng. Geol. Soc. Territ.* **2015**, *2*, 1337–1340. [CrossRef]
15. Frigerio, S.; Schenato, L.; Bossi, G.; Cavalli, M.; Mantovani, M.; Marcato, G.; Pasuto, A. A Web-Based Platform for Automatic and Continuous Landslide Monitoring: The Rotolon (Eastern Italian Alps) Case Study. *Comput. Geosci.* **2014**, *63*, 96–105. [CrossRef]

16. Baldi, P.; Cenni, N.; Fabris, M.; Zanutta, A. Kinematics of a Landslide Derived from Archival Photogrammetry and GPS Data. *Geomorphology* **2008**, *102*, 435–444. [CrossRef]
17. Mora, O.E.; Gabriela Lenzano, M.; Toth, C.K.; Grejner-Brzezinska, D.A.; Fayne, J.V. Landslide Change Detection Based on Multi-Temporal Airborne LIDAR-Derived DEMs. *Geosciences* **2018**, *8*, 23. [CrossRef]
18. Bossi, G.; Cavalli, M.; Crema, S.; Frigerio, S.; Quan Luna, B.; Mantovani, M.; Marcato, G.; Schenato, L.; Pasuto, A. Multi-Temporal LiDAR-DTMs as a Tool for Modelling a Complex Landslide: A Case Study in the Rotolon Catchment (Eastern Italian Alps). *Nat. Hazards Earth Syst. Sci.* **2015**, *15*, 715–722. [CrossRef]
19. Jaboyedoff, M.; Oppikofer, T.; Abellán, A.; Derron, M.H.; Loye, A.; Metzger, R.; Pedrazzini, A. Use of LIDAR in Landslide Investigations: A Review. *Nat. Hazards* **2012**, *61*, 5–28. [CrossRef]
20. Tondo, M.; Mulas, M.; Ciccarese, G.; Marcato, G.; Bossi, G.; Tonidandel, D.; Mair, V.; Corsini, A. Detecting Recent Dynamics in Large-Scale Landslides via the Digital Image Correlation of Airborne Optic and LiDAR Datasets: Test Sites in South Tyrol (Italy). *Remote Sens.* **2023**, *15*, 2971. [CrossRef]
21. Squarzoni, C.; Delacourt, C.; Allemand, P. Nine Years of Spatial and Temporal Evolution of the La Valette Landslide Observed by SAR Interferometry. *Eng. Geol.* **2003**, *68*, 53–66. [CrossRef]
22. Iasio, C.; Novali, F.; Corsini, A.; Mulas, M.; Branzanti, M.; Benedetti, E.; Giannico, C.; Tamburini, A.; Mair, V. COSMO SkyMed High Frequency—High Resolution Monitoring of an Alpine Slow Landslide, Corvara in Badia, Northern Italy. In Proceedings of the 2012 IEEE International Geoscience and Remote Sensing Symposium, Munich, Germany, 22–27 July 2012; pp. 7577–7580. [CrossRef]
23. Gaidi, S.; Galve, J.P.; Melki, F.; Ruano, P.; Reyes-Carmona, C.; Marzougui, W.; Devoto, S.; Pérez-Peña, J.V.; Azañón, J.M.; Chouaieb, H.; et al. Analysis of the Geological Controls and Kinematics of the Chgega Landslide (Mateur, Tunisia) Exploiting Photogrammetry and Insar Technologies. *Remote Sens.* **2021**, *13*, 4048. [CrossRef]
24. Mateos, R.M.; Ezquerro, P.; Azañón, J.M.; Gelabert, B.; Herrera, G.; Fernández-Merodo, J.A.; Spizzichino, D.; Sarro, R.; García-Moreno, I.; Béjar-Pizarro, M. Coastal Lateral Spreading in the World Heritage Site of the Tramuntana Range (Majorca, Spain). The Use of PSInSAR Monitoring to Identify Vulnerability. *Landslides* **2018**, *15*, 797–809. [CrossRef]
25. Schlögel, R.; Thiebes, B.; Mulas, M.; Cuozzo, G.; Notarnicola, C.; Schneiderbauer, S.; Crespi, M.; Mazzoni, A.; Mair, V.; Corsini, A. Multi-Temporal x-Band Radar Interferometry Using Corner Reflectors: Application and Validation at the Corvara Landslide (Dolomites, Italy). *Remote Sens.* **2017**, *9*, 739. [CrossRef]
26. Mulas, M.; Bayer, B.; Bertolini, G.; Bonacini, F.; Leuratti, E.; Pizziolo, M.; Simoni, A.; Corsini, A. Impulsive Ground Movements in the Mud Volcanoes Area of "Le Sarse" Di Puianello (Northern Apennines, Modena, Italy): Field Evidence and Multi-Approach Monitoring. *Rend. Online Della Soc. Geol. Ital.* **2016**, *41*, 251–254. [CrossRef]
27. Peyret, M.; Djamour, Y.; Rizza, M.; Ritz, J.-F.; Hurtrez, J.-E.; Goudarzi, M.A.; Nankali, H.; Chéry, J.; Le Dortz, K.; Uri, F. Monitoring of the Large Slow Kahrod Landslide in Alborz Mountain Range (Iran) by GPS and SAR Interferometry. *Eng. Geol.* **2008**, *100*, 131–141. [CrossRef]
28. Bovenga, F.; Pasquariello, G.; Pellicani, R.; Refice, A.; Spilotro, G. Landslide Monitoring for Risk Mitigation by Using Corner Reflector and Satellite SAR Interferometry: The Large Landslide of Carlantino (Italy). *Catena* **2017**, *151*, 49–62. [CrossRef]
29. Mulas, M.; Corsini, A.; Cuozzo, G.; Callegari, M.; Thiebes, B.; Mair, V. Quantitative Monitoring of Surface Movements on Active Landslides by Multi-Temporal, High-Resolution X-Band SAR Amplitude Information: Preliminary Results. In *Landslides and Engineered Slopes. Experience, Theory and Practice*; CRC Press: Boca Raton, FL, USA, 2016; pp. 1511–1516. [CrossRef]
30. Qu, T.; Lu, P.; Liu, C.; Wu, H.; Shao, X.; Wan, H.; Li, N.; Li, R. Hybrid-SAR Technique: Joint Analysis Using Phase-Based and Amplitude-Based Methods for the Xishancun Giant Landslide Monitoring. *Remote Sens.* **2016**, *8*, 874. [CrossRef]
31. Wang, M.; Zhou, J.; Chen, J.; Jiang, N.; Zhang, P.; Li, H. Automatic Identification of Rock Discontinuity and Stability Analysis of Tunnel Rock Blocks Using Terrestrial Laser Scanning. *J. Rock Mech. Geotech. Eng.* **2023**, *15*, 1810–1825. [CrossRef]
32. Abellán, A.; Calvet, J.; Vilaplana, J.M.; Blanchard, J. Detection and Spatial Prediction of Rockfalls by Means of Terrestrial Laser Scanner Monitoring. *Geomorphology* **2010**, *119*, 162–171. [CrossRef]
33. Corsini, A.; Castagnetti, C.; Bertacchini, E.; Rivola, R.; Ronchetti, F.; Capra, A. Integrating Airborne and Multi-temporal Long-range Terrestrial Laser Scanning with Total Station Measurements for Mapping and Monitoring a Compound Slow Moving Rock Slide. *Earth Surf. Process Landf.* **2013**, *38*, 1330–1338. [CrossRef]
34. Giordan, D.; Hayakawa, Y.; Nex, F.; Remondino, F.; Tarolli, P. Review Article: The Use of Remotely Piloted Aircraft Systems (RPASs) for Natural Hazards Monitoring and Management. *Nat. Hazards Earth Syst. Sci.* **2018**, *18*, 1079–1096. [CrossRef]
35. Thiebes, B.; Tomellari, E.; Mejia-Aguilar, M.; Rabanser, M.; Schlögel, R.; Mulas, M.; Corsini, A. Assessment of the 2006 to 2015 Corvara Landslide Evolution a UAV-Derived DSM and Orthophoto. In *Landslides and Engineered Slopes. Experience, Theory and Practice*; CRC Press: Boca Raton, FL, USA, 2018; pp. 1897–1902. [CrossRef]
36. Sestras, P.; Bilașco, Ș.; Roșca, S.; Dudic, B.; Hysa, A.; Spalević, V. Geodetic and UAV Monitoring in the Sustainable Management of Shallow Landslides and Erosion of a Susceptible Urban Environment. *Remote Sens.* **2021**, *13*, 385. [CrossRef]
37. Mugnai, F.; Tucci, G. A Comparative Analysis of Unmanned Aircraft Systems in Low Altitude Photogrammetric Surveys. *Remote Sens.* **2022**, *14*, 726. [CrossRef]
38. Westoby, M.J.; Brasington, J.; Glasser, N.F.; Hambrey, M.J.; Reynolds, J.M. "Structure-from-Motion" Photogrammetry: A Low-Cost, Effective Tool for Geoscience Applications. *Geomorphology* **2012**, *179*, 300–314. [CrossRef]

39. Peppa, M.V.; Mills, J.P.; Moore, P.; Miller, P.E.; Chambers, J.E. Automated Co-registration and Calibration in SfM Photogrammetry for Landslide Change Detection. *Earth Surf. Process Landf.* **2019**, *44*, 287–303. [CrossRef]
40. Godone, D.; Allasia, P.; Borrelli, L.; Gullà, G. UAV and Structure from Motion Approach to Monitor the Maierato Landslide Evolution. *Remote Sens.* **2020**, *12*, 1039. [CrossRef]
41. Eker, R.; Alkan, E.; Aydin, A. A Comparative Analysis of UAV-RTK and UAV-PPK Methods in Mapping Different Surface Types. *Eur. J. For. Eng.* **2021**, *7*, 12–25. [CrossRef]
42. Tavani, S.; Granado, P.; Riccardi, U.; Seers, T.; Corradetti, A. Terrestrial SfM-MVS Photogrammetry from Smartphone Sensors. *Geomorphology* **2020**, *367*, 107318. [CrossRef]
43. Mazza, D.; Romeo, S.; Cosentino, A.; Mazzanti, P.; Guadagno, F.M.; Revellino, P. The Contribution of Digital Image Correlation for the Knowledge, Control and Emergency Monitoring of Earth Flows. *Geosciences* **2023**, *13*, 364. [CrossRef]
44. Casagli, N.; Frodella, W.; Morelli, S.; Tofani, V.; Ciampalini, A.; Intrieri, E.; Raspini, F.; Rossi, G.; Tanteri, L.; Lu, P. Spaceborne, UAV and Ground-Based Remote Sensing Techniques for Landslide Mapping, Monitoring and Early Warning. *Geoenviron. Disasters* **2017**, *4*, 9. [CrossRef]
45. Tang, C.; Wang, Y.; Zhang, L.; Zhang, Y. GNSS/Inertial Navigation/Wireless Station Fusion UAV 3-D Positioning Algorithm With Urban Canyon Environment. *IEEE Sens. J.* **2022**, *22*, 18771–18779. [CrossRef]
46. Martínez-Carricondo, P.; Agüera-Vega, F.; Carvajal-Ramírez, F. Accuracy Assessment of RTK/PPK UAV-Photogrammetry Projects Using Differential Corrections from Multiple GNSS Fixed Base Stations. *Geocarto Int.* **2023**, *38*, 2197507. [CrossRef]
47. Taddia, Y.; Stecchi, F.; Pellegrinelli, A. Using DJI Phantom 4 RTK Drone for Topographic Mapping of Coastal Areas. *Int. Arch. Photogramm. Remote Sens. Spat. Inf. Sci.* **2019**, *XLII-2/W13*, 625–630. [CrossRef]
48. Kalacska, M.; Lucanus, O.; Arroyo-Mora, J.P.; Laliberté, É.; Elmer, K.; Leblanc, G.; Groves, A. Accuracy of 3d Landscape Reconstruction without Ground Control Points Using Different Uas Platforms. *Drones* **2020**, *4*, 13. [CrossRef]
49. Stott, E.; Williams, R.D.; Hoey, T.B. Ground Control Point Distribution for Accurate Kilometre-Scale Topographic Mapping Using an Rtk-Gnss Unmanned Aerial Vehicle and Sfm Photogrammetry. *Drones* **2020**, *4*, 55. [CrossRef]
50. Peppa, M.V.; Hall, J.; Goodyear, J.; Mills, J.P. Photogrammetric Assessment and Comparison of Dji Phantom 4 pro and Phantom 4 Rtk Small Unmanned Aircraft Systems. *Int. Arch. Photogramm. Remote Sens. Spat. Inf. Sci. ISPRS Arch.* **2019**, *42*, 503–509. [CrossRef]
51. Notti, D.; Giordan, D.; Cina, A.; Manzino, A.; Maschio, P.; Bendea, I.H. Debris Flow and Rockslide Analysis with Advanced Photogrammetry Techniques Based on High-Resolution RPAS Data. Ponte Formazza Case Study (NW Alps). *Remote Sens.* **2021**, *13*, 1797. [CrossRef]
52. Cruden, D.M.; Varnes, D.J. Landslide Types and Processes. In *Landslides: Investigation and Mitigation*; Volume Special Report 247; National Academy Press: Washington, DC, USA, 1996; pp. 36–75, ISBN 030906208X.
53. Corsini, A.; Borgatti, L.; Caputo, G.; De Simone, N.; Sartini, G.; Truffelli, G. Investigation and Monitoring in Support of the Structural Mitigation of Large Slow Moving Landslides: An Example from Ca' Lita (Northern Apennines, Reggio Emilia, Italy). *Nat. Hazards Earth Syst. Sci.* **2006**, *6*, 55–61. [CrossRef]
54. Borgatti, L.; Corsini, A.; Barbieri, M.; Sartini, G.; Truffelli, G.; Caputo, G.; Puglisi, C. Large Reactivated Landslides in Weak Rock Masses: A Case Study from the Northern Apennines (Italy). *Landslides* **2006**, *3*, 115–124. [CrossRef]
55. Mulas, M.; Ciccarese, G.; Truffelli, G.; Corsini, A. Integration of Digital Image Correlation of Sentinel-2 Data and Continuous GNSS for Long-Term Slope Movements Monitoring in Moderately Rapid Landslides. *Remote Sens.* **2020**, *12*, 2605. [CrossRef]
56. Antolini, G.; Auteri, L.; Pavan, V.; Tomei, F.; Tomozeiu, R.; Marletto, V. A Daily High-Resolution Gridded Climatic Data Set for Emilia-Romagna, Italy, during 1961–2010. *Int. J. Climatol.* **2016**, *36*, 1970–1986. [CrossRef]
57. Arpae Agenzia Prevenzione Ambiente Energia Emilia-Romagna. Tabelle Climatologiche. Available online: https://www.arpae.it/it/temi-ambientali/clima/dati-e-indicatori/tabelle-climatiche (accessed on 4 March 2024).
58. Köppen, W. Das Geographische System Der Klimate. In *Handbuch der Klimatologie*; Gebrüder Borntraeger: Berlin, Germany, 1936.
59. Borgatti, L.; Corsini, A.; Marcato, G.; Ronchetti, F.; Zabuski, L. Appraise the Structural Mitigation of Landslide Risk via Numerical Modelling: A Case Study from the Northern Apennines (Italy). *Georisk* **2008**, *2*, 141–160. [CrossRef]
60. Cervi, F.; Ronchetti, F.; Martinelli, G.; Bogaard, T.A.; Corsini, A. Origin and Assessment of Deep Groundwater Inflow in the Ca' Lita Landslide Using Hydrochemistry and in Situ Monitoring. *Hydrol. Earth Syst. Sci.* **2012**, *16*, 4205–4221. [CrossRef]
61. Ronchetti, F.; Borgatti, L.; Cervi, F.; Corsini, A. Hydro-Mechanical Features of Landslide Reactivation in Weak Clayey Rock Masses. *Bull. Eng. Geol. Environ.* **2010**, *69*, 267–274. [CrossRef]
62. Mulas, M.; Ciccarese, G.; Truffelli, G.; Corsini, A. Displacements of an Active Moderately Rapid Landslide—A Dataset Retrieved by Continuous GNSS Arrays. *Data* **2020**, *5*, 71. [CrossRef]
63. Corsini, A.; Bonacini, F.; Mulas, M.; Ronchetti, F.; Monni, A.; Pignone, S.; Primerano, S.; Bertolini, G.; Caputo, G.; Truffelli, G.; et al. A Portable Continuous GPS Array Used as Rapid Deployment Monitoring System during Landslide Emergencies in Emilia Romagna. *Rend. Online Della Soc. Geol. Ital.* **2015**, *35*, 89–91. [CrossRef]
64. Brooke-Holland, L. *Unmanned Aerial Vehicles (Drones): An Introduction*; House of Commons Library: London, UK, 2012.
65. Turner, A.K.; Schuster, R.L. *Landslides: Investigation and Mitigation*; Volume Special Report 247; National Academy Press: Washington, DC, USA, 1996; ISBN 030906208X.

66. Mugnai, F.; Angelini, R.; Cortesi, I.; Masiero, A. Integrating UAS Photogrammetry and Digital Image Correla-Tion for High-Resolution Monitoring of Large Landslides. *Preprints* **2022**. [CrossRef]
67. Everett, M.E.; DeSmet, T.S.; Warden, R.R.; Ruiz-Guzman, H.A.; Gavette, P.; Hagin, J. The Fortress beneath: Ground Penetrating Radar Imaging of the Citadel at Alcatraz: 1. A Guide for Interpretation. *Heritage* **2021**, *4*, 1328–1347. [CrossRef]